

# Improved Sequentially Processed Cu(In,Ga)(S,Se)<sub>2</sub> by Ag Alloying

Aubin Jean-Claude Mireille Prot,\* Michele Melchiorre, Tilly Schaaf, Ricardo Gonçalves Poeira, Hossam Elanzeery, Alberto Lomuscio, Souhaib Oueslati, Anastasia Zelenina, Thomas Dalibor, Gunnar Kusch, Yucheng Hu, Rachel Angharad Oliver, and Susanne Siebentritt

**Alloying small quantities of silver into Cu(In,Ga)Se<sub>2</sub> is shown to improve the efficiency for wide and low bandgap solar cells. Low bandgap industrial Cu(In,Ga)(S,Se)<sub>2</sub> absorbers are studied, substituting less than 10% of the copper with silver, using absolute photoluminescence and cathodoluminescence spectroscopy. Silver improves the grain size and promotes the interdiffusion of Ga and In across the depth of the absorber, resulting in a smoother bandgap gradient. However, a certain lateral inhomogeneity is observed near the front and back sides. The nonradiative losses in the bare absorbers are reduced by up to 30 meV.**

## 1. Introduction

Reaching a record power conversion efficiency (PCE) of 23.6%,<sup>[1]</sup> chalcopyrite solar cells are one of the best thin film technologies for solar power harvesting. The efficiency record has been achieved with a Cu(In,Ga)Se<sub>2</sub> (CIGS)-based solar cell, in which some of the Cu was replaced by silver (Ag). It is generally observed that Ag improves the optoelectronic quality of the CIGS solar cell.<sup>[2]</sup> Alloying with Ag decreases both the conduction ( $E_C$ ) and valence ( $E_V$ ) band energy.<sup>[3]</sup>  $E_V$  decreases first slower than  $E_C$  until a certain  $[Ag]/([Ag] + [Cu])$  ratio (or AAC) is reached before the opposite happens. This results in a decrease

of the bandgap for low AAC and an increase for high AAC.<sup>[3]</sup> Depending on the  $[Ga]/([Ga] + [In])$  ratio (or GGI), the change in bandgap is more or less pronounced. According to Keller et al. a small amount of Ag (AAC < 0.25) has a stronger effect (decrease of  $E_g$ ) on a wider bandgap material than on a lower bandgap one, whose  $E_g$  is barely affected at low AAC.<sup>[3]</sup>

Growing Ag-based solar cell has been done for nearly two decades already. In 2005, Nakada et al. achieved a 9.2% PCE for a 1.7 eV bandgap Ag(In,Ga)Se<sub>2</sub> solar

cell.<sup>[4]</sup> More recently, several studies reported on alloying Ag with wide bandgap Cu(In,Ga)Se<sub>2</sub> (ranging from  $E_g = 1.24$  eV to  $E_g = 1.46$  eV) during coevaporation,<sup>[5–9]</sup> improving the performances mostly by increasing the  $V_{OC}$ . Improving such wide gap material would be interesting for multijunction devices. At the same time, the effect of Ag alloying is also actively investigated in lower bandgap Cu(In,Ga)Se<sub>2</sub> (ranging from  $E_g = 1.02$  eV to  $E_g = 1.18$  eV).<sup>[10–14]</sup> Leading to a lower melting temperature than the pure Cu compounds,<sup>[15]</sup> alloying with Ag offers the possibility to process the absorbers at lower temperature, which represents a great advantage from an industrial point of view. Alternatively, growing at similar temperatures as the Ag-free compound, grain size can be increased<sup>[15]</sup> and crystal defects may be reduced as simulated in Zhang et al.<sup>[16]</sup> The presence of Ag in the crystal lattice has the following reported effects: an improved morphology is widely observed, translated into an increase of the grain size,<sup>[17]</sup> a smoother surface<sup>[14]</sup> is commonly obtained, and in low bandgap absorbers, deep defects may be passivated.<sup>[18]</sup> In addition, a reduction of the doping—hole density—and an improved current collection are systematically reported and attributed to a widening of the space charge region.<sup>[12]</sup> The optimum amount of Ag necessary to obtain improved device performance depends strongly on the composition of the host material, i.e., the GGI and  $([Ag] + [Cu])/([Ga] + [In])$  (or I/III) ratios, explaining the large discrepancies observed in the literature regarding the best cells' AAC ratio.


Ag alloying has been tried in Cu(In,Ga)S<sub>2</sub> (sulfide) absorbers as well. Mori et al. showed improved absorber quality (of bandgaps ranging from 1.54 to 1.66 eV) and larger short-circuit current ( $J_{SC}$ ), but also reported a lower open circuit voltage ( $V_{OC}$ ) which ultimately led to a decreased cell efficiency.<sup>[19]</sup> Cheng et al. first prepared a (Ag,Cu)(In,Ga)Se<sub>2</sub> solar cell that showed improved

A. J. C. M. Prot, M. Melchiorre, T. Schaaf, S. Siebentritt  
Laboratory for Photovoltaics, Physics and Materials Science Research Unit  
University of Luxembourg  
41 rue du Brill, L-4422 Belvaux, Luxembourg  
E-mail: aubin.prot@uni.lu

R. G. Poeira  
Laboratory for Energy Materials, Physics and Materials Science  
Research Unit  
University of Luxembourg  
41 rue du Brill, L-4422 Belvaux, Luxembourg

H. Elanzeery, A. Lomuscio, S. Oueslati, A. Zelenina, T. Dalibor  
AVANCIS GmbH  
Otto-Hahn-Ring 6, 81739 München, Germany

G. Kusch, Y. Hu, R. A. Oliver  
Department of Materials Science and Metallurgy  
University of Cambridge  
27 Charles Babbage Road, Cambridge CB3 0FS, UK

 The ORCID identification number(s) for the author(s) of this article can be found under <https://doi.org/10.1002/solr.202400208>.

DOI: 10.1002/solr.202400208

performances and subsequently sulfurized the absorber, forming  $(\text{Ag,Cu})(\text{In,Ga})(\text{S,Se})_2$  ( $E_g = 1.02$  eV) which further improved the performance.<sup>[20]</sup>

While previous research predominantly focused on selenide absorbers, the literature on sulfur–selenide absorbers alloyed with Ag remains to this day relatively sparse. This work aims to bridge this gap by investigating how Ag incorporation affects the elemental composition and performance of  $\text{Cu}(\text{In,Ga})(\text{S,Se})_2$  absorbers (CIGSSe). Different (low) amounts of Ag are introduced as precursor in the elemental stack of industrial CIGSSe. The bare absorbers are optically characterized, specifically by photoluminescence (PL) and cathodoluminescence (CL) spectroscopy, revealing an enhanced interdiffusion of Ga and In following Ag alloying. The absorbers' nonradiative losses are reduced, and the electrical performance of the resulting solar cells is measured.

## 2. Results and Discussion

The effect of Ag alloying on the film morphology and performances of CIGSSe absorbers is reported in the following subsections. The enhanced interdiffusion of In and Ga and the resulting lateral inhomogeneity is further discussed by means of PL, CL, and Raman spectroscopy.

### 2.1. Effect on the Crystal Structure

Scanning electron microscope (SEM) imaging of the top surface and cross section of the samples is performed. **Figure 1** shows the images for the reference sample and the samples Ag-1 and Ag-3 (lowest and highest Ag content, see Table 1 in the Experimental Section). From the cross-sectional images (Figure 1 bottom) an overall increase in the grain size is observed

as more Ag is added, comparatively with the reference sample. With the highest Ag content, grains larger than  $2\ \mu\text{m}$  are obtained. This is expected as Ag has a lower melting point than Cu and thus growing  $(\text{Ag,Cu})(\text{In,Ga})(\text{S,Se})_2$  at similar temperature as the pure Cu-compound results in larger grains.<sup>[15]</sup> Moreover, in the reference sample, a layer of fine grains is present near the back contact. With increasing Ag content, the size of these fine grains increases until no strong contrast between them and the bulk ones is visible anymore. This is consistent with the observations reported in ref. [14].

The top-view SEM images (Figure 1 top) also reveal morphology modifications with added Ag. The reference sample exhibits a relatively smooth surface. With the lowest Ag content (Ag-1), crevices appear on the surface and further adding Ag (Ag-3) leads to an increased density of these crevices. Essig et al. reported similar features in coevaporated  $(\text{Ag,Cu})(\text{In,Ga})\text{Se}_2$  absorbers, speculating that they are related to the agglomeration of Ag on the surface during deposition.<sup>[21]</sup> However, they show that these crevices remain shallow or inexistent for low Ag contents (AAC  $\approx 0.05$ ) and do not impact the cell performance. Would the crevices be deep enough to connect with the back contact, the shunt resistance would tend to zero and the device would not work. In the present case, the crevices seem to be nondetrimental from an optical characterization point of view, as discussed in the next section.

### 2.2. Composition Investigation

The in-depth composition of the absorbers has been investigated by glow discharge optical emission spectroscopy (GDOES) and the GGI profiles of the three samples shown in Figure 1 are reported in **Figure 2**. The samples are grown with an intentional bandgap gradient, leading to a profile like the reference one (green line): a low GGI near the front and an increasing GGI

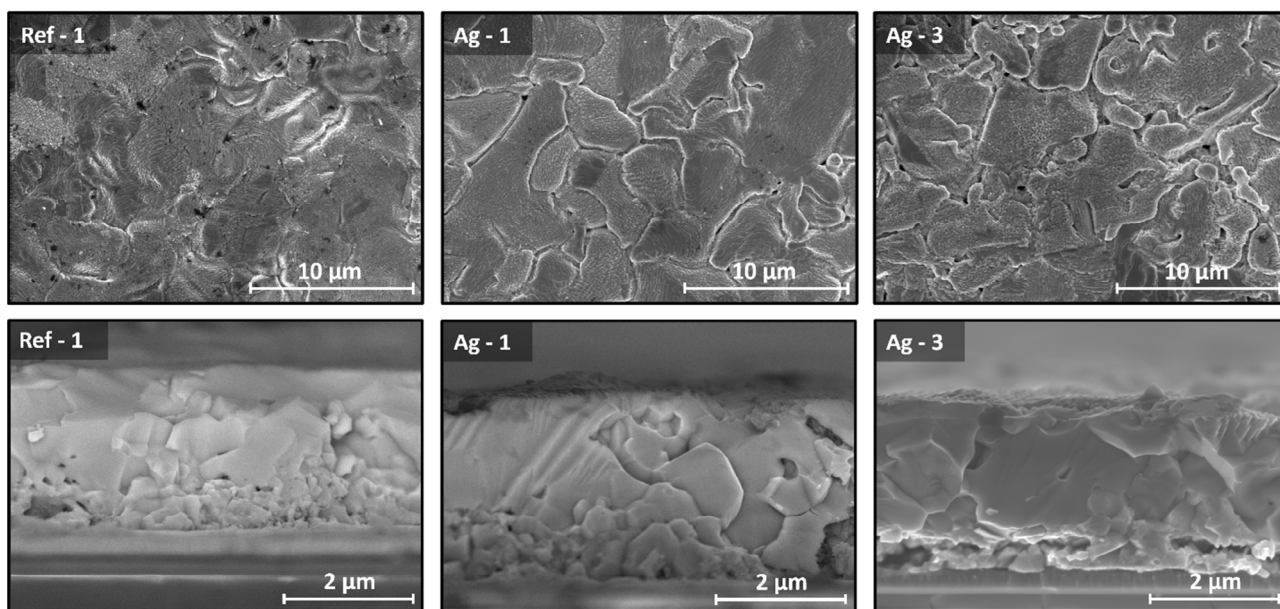


**Figure 1.** SEM images of top view (top) and cross section (bottom) of the reference absorber, containing no Ag, and two absorbers with low Ag content (Ag-1) and high Ag content (Ag-3). The sample Ag-3 is slightly detached from the substrate, most probably due to imperfect cleaving.

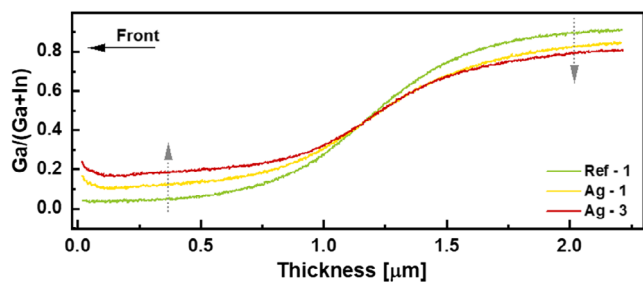


**Figure 2.** GGI profiles as measured by GDOES for the three absorbers shown in Figure 1. With increasing Ag content, the profiles flatten.

toward the back side. It has been demonstrated in a previous report (on similar CIGS<sub>Se</sub> absorbers without Ag) that in fact no smooth bandgap increase generally exists. Instead, two phases of low GGI (low gap phase) and high GGI (high gap phase) form at the front and back side, respectively, and interlace in the bulk of the absorber.<sup>[22]</sup> This results in the average GGI profile depicted in Figure 2.

Upon addition of Ag, the GGI profiles flatten. The overall GGI at the notch position ( $E_{g,min}$ , from  $\approx 100$  to  $\approx 700$  nm) increases from below 0.1 to 0.2 while the GGI at the back (over the last 400 nm) decreases from 0.9 to 0.8. Such flattening of the GGI profiles has been reported in low and high bandgap Ag-alloyed chalcopyrites.<sup>[3,13]</sup> This suggests that Ag enhances the interdiffusion of Ga and In, as reported in ref. [23]. Based on these profiles, a low gap phase of higher  $E_g$  is expected toward the front surface, and a high gap phase of lower  $E_g$  is expected near the back contact. This is discussed in more details in Section 2.3 and 2.4. All the absorbers have been probed on four different spots and yield very similar profiles, attesting to the homogeneity of the samples. Exception is the sample Ag-3 for which the greatest discrepancies have been observed (Figure S1.1, Supporting Information), hinting that higher Ag content may reduce the lateral homogeneity. It has been demonstrated that diffusion of Ga and In in CIGS occurs through Cu vacancies.<sup>[24,25]</sup> Based on the diffusion model proposed in,<sup>[26]</sup> atom diffusion (in particular, Ga and In) may be enhanced or hindered by the presence of dopants, depending on the concentration of dopant and vacancies. Because Ag sits on the same sites as Cu, it may reduce the concentration of  $V_{Cu}$

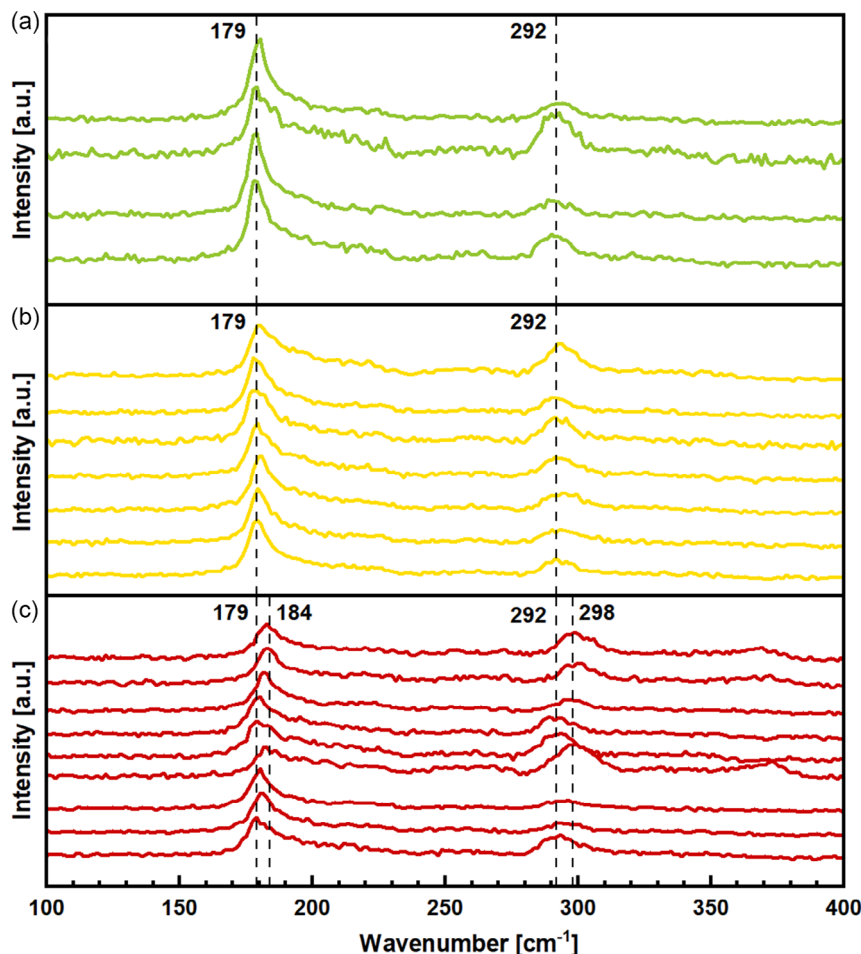


**Figure 3.** a) Raman spectroscopy performed on the reference sample, b) the sample Ag-1 with the lowest Ag content, and c) Ag-3 with the highest Ag content. Each spectrum corresponds to a different spot on the sample. The spectra are normalized to the Se–Se peak and manually shifted for display purpose.

(provided that the I/III ratio changes) and, in too great amounts, alter the diffusion, leading to compositional inhomogeneities, as observed in Ag-3. As indicated in the Experimental Section, however, no significant change in the I/III is measured. Additionally, the S/(S + Se) profiles indicate a slight overall increase of the S content for all Ag-alloyed samples (Figure S1.2, Supporting Information).

The lateral inhomogeneity of the high-Ag sample is confirmed by Raman spectroscopy. Figure 3 displays the spectra obtained from the front side of the samples Ag-1 (yellow) and Ag-3 (red) on different spots, compared to the reference sample without Ag (green). The latter shows two main peaks, associated to the A-like symmetry modes of the Se–Se and S–S vibrations, at  $179\text{ cm}^{-1}$  and  $292\text{ cm}^{-1}$ , respectively.<sup>[27,28]</sup> The sample Ag-1 (lowest Ag content) yields the same two peaks, showing no significant difference to the reference sample. However, in the case of the sample Ag-3 (highest Ag content), these peaks are shifting in energy between different positions while scanning the surface, without showing any broadening. The Se–Se peak shifts from  $179\text{ cm}^{-1}$  to  $184\text{ cm}^{-1}$  together with the S–S peak from  $292$  to  $298\text{ cm}^{-1}$ . Such a shift is usually associated with increased Ga content.<sup>[29]</sup> Thus, this observation could indicate the formation of (Ag,Cu)(In,Ga)(S,Se) phases of higher Ga content close to the surface in addition to the same low gap phase as the reference (producing the peaks at  $179$  and  $292\text{ cm}^{-1}$ ). The formation of phases of higher bandgap explains the increase in the GGI ratio observed toward the front side.

It is usually observed that (Ag,Cu)(In,Ga)Se<sub>2</sub> solar cells have a low tolerance to (Ag,Cu)-poor off-stoichiometry composition,<sup>[30]</sup> leading to the formation of ordered vacancy compounds (OVC). Keller et al. show that OVCs form for I/III ratios < 0.97. Above this value, other secondary phases start appearing as

stoichiometry is approached. Both OVC and secondary phases are detrimental to the device performance.<sup>[7]</sup> In this study, no OVC signature in the Raman spectra is present in either sample.

### 2.3. PL Spectroscopy

The bare absorbers are investigated by absolute PL from the front and back sides (see Figure 4). A soft KCN etching (5% concentration for 30 sec) is performed before measuring from the front side to remove oxides and refresh the surface after the absorbers have been exposed to air. The back side is accessed after performing a mechanical lift-off of the absorber from its substrate, similar to ref. [22]. PL spectra provide information about the recombination activity in the material. The reference sample in this study is a CIGSSe absorber with a bandgap around 1.05 eV. Therefore, a dominant PL peak is expected at this specific energy and is attributed to band-to-band recombination (Figure 4, Ref-1). As already deduced from the Raman analysis, the Ag-alloyed samples have the same low gap phase as the reference. The PL analysis confirms it because the same emission at 1.05 eV is observed for samples Ag-1 and Ag-3 from the front side. This is coherent with the theoretical bandgap predictions for selenides computed in ref. [3] for both low Ga and low Ag contents. However, with the highest Ag content (Figure 4, Ag-3), a shoulder is seen at higher energies ( $\approx 1.25\text{ eV}$ ) from the front side and suggests the presence of an alternative recombination channel. The possibility of forming OVCs and/or secondary phases is discussed extensively for high bandgap CIGSe in ref. [30], reporting principally the formation of 1:3:5 OVCs ((Ag,Cu)(Ga,In)<sub>3</sub>Se<sub>5</sub>) at the front and back interfaces for I/III off-stoichiometry absorbers. Close to stoichiometry, the authors observed the formation of sparse Ag<sub>3</sub>GaSe<sub>6</sub> grains, which are,

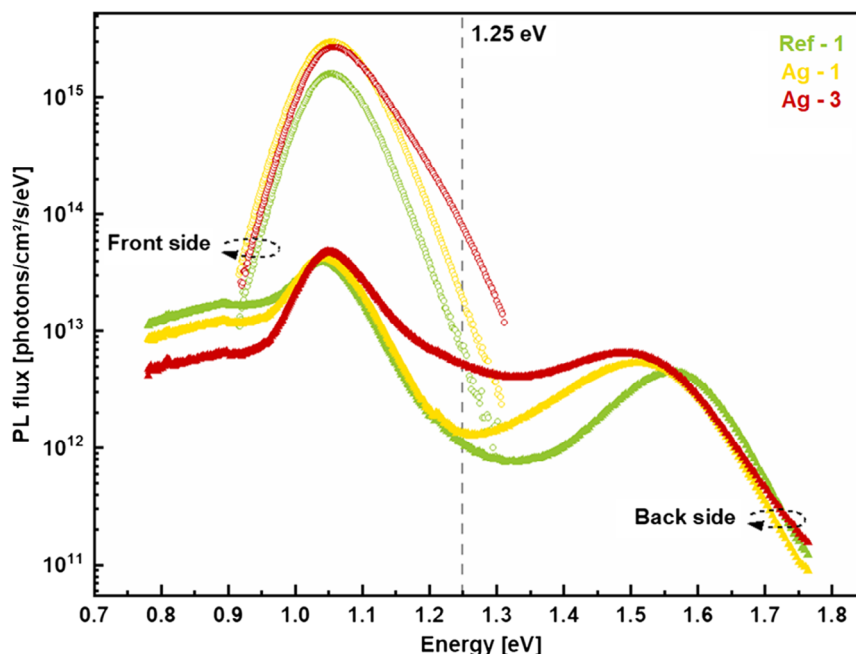


**Figure 4.** Absolute PL measured from the front (open circles) and back (full triangles) sides of the reference sample (green) and the samples Ag-1 (yellow) and Ag-3 (red). No high energy peak is observed from the front side and the part where  $E > 1.3\text{ eV}$  is not displayed. Note that the y-axis is in logarithmic scale.

however, mainly expected for above stoichiometry compounds. In the present case, despite the relatively low I/III ratio, only (A)CIGSSe phases and no OVC phases were detected from Raman spectroscopy, suggesting that the shoulder in the PL comes from an (A)CIGSSe phase of higher GGI than the low gap phase. The formation of this additional phase reinforces the statement that Ga diffuses through the absorber with Ag alloying.

Measurement from the back side reveals two main emission peaks. The one at low energy corresponds to the notch emission, similarly as from the front side measurement. The PL intensity is, however, lower by almost two orders of magnitude. This reduction may arise from several factors: 1) part of the carriers participate to the emission at higher energy; 2) only a fraction of the carriers generated at the back side can reach the notch due to the higher nonradiative recombination rate of back side, as demonstrated in ref. [31]; and 3) the imperfect lift-off procedure might introduce further nonradiative recombination channels. SEM top-view images of the back side of the absorbers are provided in Figure S6, Supporting Information.

The second emission peak has been demonstrated to arise from the high gap phase forming near the back side of graded absorbers.<sup>[22]</sup> Although the three absorbers in Figure 4 were grown with the same amount of Ga and In precursors, the bandgap of the high gap phase, dependent on the GGI at the back side, reduces with increasing Ag content (from 1.56 to 1.49 eV). Furthermore, the valley between the two peaks becomes shallower for higher Ag contents and the same shoulder at  $\approx 1.25$  eV is detected for the sample Ag-3. This supports the earlier claim that the diffusion of Ga is enhanced by Ag alloying and additional evidence is provided by CL in Section 2.4. The relation between the back side GGI and the PL maximum of the high gap phase follows well the trend previously observed in ref. [22] (see Figure S2, Supporting Information). From the back side (Figure 4), a broad PL contribution is observed below 0.9 eV

and attributed to a deep defect associated with the high gap phase forming near the back side of the absorbers.<sup>[22]</sup>

From absolute PL measurement on the front side, information about quasi-Fermi-level splitting (qFLs), tail states, bandgap fluctuations, and optical diode factor (ODF) can be obtained and are discussed in the following. QFLs gives an upper limit to the open-circuit voltage ( $V_{OC}$ ) and is therefore a very useful quantity to anticipate how good a finished cell can be.<sup>[32]</sup> Fitting the high energy part of the PL spectrum, sufficiently far above the bandgap—where it is assumed that the absorptance is equal to 1—one can get a measure of the qFLs.<sup>[33]</sup> However, because of the shoulder in this range (see Figure 4), we opted for an evaluation of the qFLs based on the PL quantum yield ( $Y_{PL}$ , referred as ERE in ref. [33]) following Equation (1):

$$qFLs = eV_{OC}^{SQ} - kT \cdot \ln(Y_{PL}) \quad (1)$$

with  $V_{OC}^{SQ}$  the Shockley–Queisser  $V_{OC}$  where the energy of the PL maximum is taken as the bandgap and a perfect back reflector is considered.<sup>[34,35]</sup>  $e$  is the elementary charge,  $k$  is the Boltzmann constant,  $T$  is the temperature, and finally  $Y_{PL}$  is the PL quantum yield defined as the ratio between the emitted photon flux and the absorbed one. Moreover, the quantity  $kT \cdot \ln(Y_{PL})$  represents the nonradiative losses and, contrary to the qFLs, does not depend on the bandgap of the material, allowing for a comparison of absorbers with different bandgaps. In addition to the three samples considered up to this point, four samples of intermediate Ag content but lower GGI in precursor stack are discussed (samples Ag-2.1–Ag-2.4, see Table 1). Reducing the GGI has been demonstrated beneficial in other studies<sup>[22,31,36]</sup> and leads to further improvement in the present one. The GGI in the precursor stack of sample Ag-2.1 is lower than the one of the reference and is further reduced for the samples Ag-2.2, Ag-2.3, and Ag-2.4 (Table 1). Samples Ag-2.2 and Ag-2.3 are identical from a composition point of view, but the temperature of the rapid

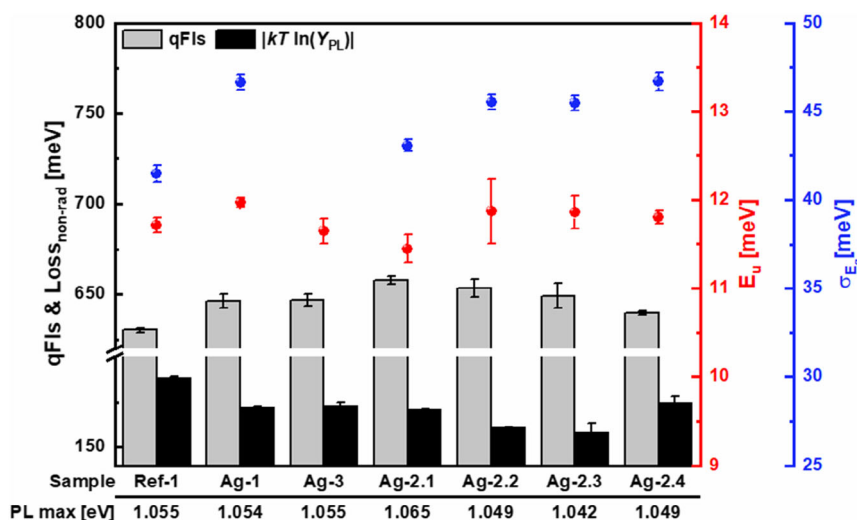


**Figure 5.** Summary of the PL results for seven samples. The samples Ag-2.1–Ag-2.4 are samples with an Ag content between Ag-1 and Ag-3. The left axis is the qFLs and the nonradiative losses defined by  $|kT \cdot \ln(Y_{PL})|$ . The first right axis (red) is the Urbach energy and the second one (blue) is the standard deviation from the mean bandgap as defined in Equation (2). The energy of the PL peak maximum (used to calculate the qFLs) is given for each sample below the bottom axis.

thermal process (RTP) of the second one is reduced. Finally, the sample Ag-2.4 is grown with a reduced Na content in the precursor stack.

**Figure 5** summarizes the results from the front side PL measurements. The highest nonradiative losses are recorded for the reference sample (188 meV). Alloying with Ag reduces these losses by 14–16 meV in the case of the samples Ag-1, Ag-3, Ag-2.1, and Ag-2.4 and a decrease by as much as 30 meV is achieved for the samples Ag-2.2 and Ag-2.3. Similar improvement would therefore be expected in the  $V_{OC}$  of a cell made from these absorbers.

As shown in **Figure 6d**, an increase in the  $V_{OC}$  is generally obtained (within error) for cells based on the investigated absorbers. However, the  $V_{OC}$  improvement does not always correlate with the reduction of the nonradiative losses measured on the bare absorbers by PL. It is important to note that while the measurements of the bare absorbers are performed on inch by inch samples (cut from larger absorbers), the *IV* parameters are measured on 10cm × 10cm encapsulated submodules. The potential effect of Ag on the buffer and window layers is not investigated in this work but could contribute to the discrepancies between PL

and *IV* results. The  $V_{OC}$  improvement for the sample Ag-2.2 is lesser than the expected one and no improvement for the sample Ag-2.3 is measured. This implies that additional losses may occur while completing the cell. Furthermore, the highest  $V_{OC}$  is measured for the sample Ag-3 (relative improvement of 6.5% compared to the reference sample's  $V_{OC}$ ) and even exceeds the corresponding qFls. Such behavior has been previously reported in ref. [33]. Despite the higher  $V_{OC}$ , the cells did not show significant improvement in efficiency, mostly due to a reduction of the short circuit current density  $J_{SC}$  (Figure 6c), leading to a lower product  $J_{SC} \cdot V_{OC}$ . The current losses may arise from the higher bandgap observed at the front side, as measured from external quantum efficiency (EQE) (see Figure S3, Supporting Information), and further discussed in Section 2.4. The best performing Ag-alloyed cell (based on absorber Ag-2.4) shows a relative improvement of 1.6% in average efficiency compared to the reference (slight improvement in  $V_{OC}$  and  $J_{SC}$  but decrease in fill factor [FF]). It can be expected that further optimization of the industrial processes for Ag containing absorbers will make full use of the reduced nonradiative recombination and result in improved efficiencies.

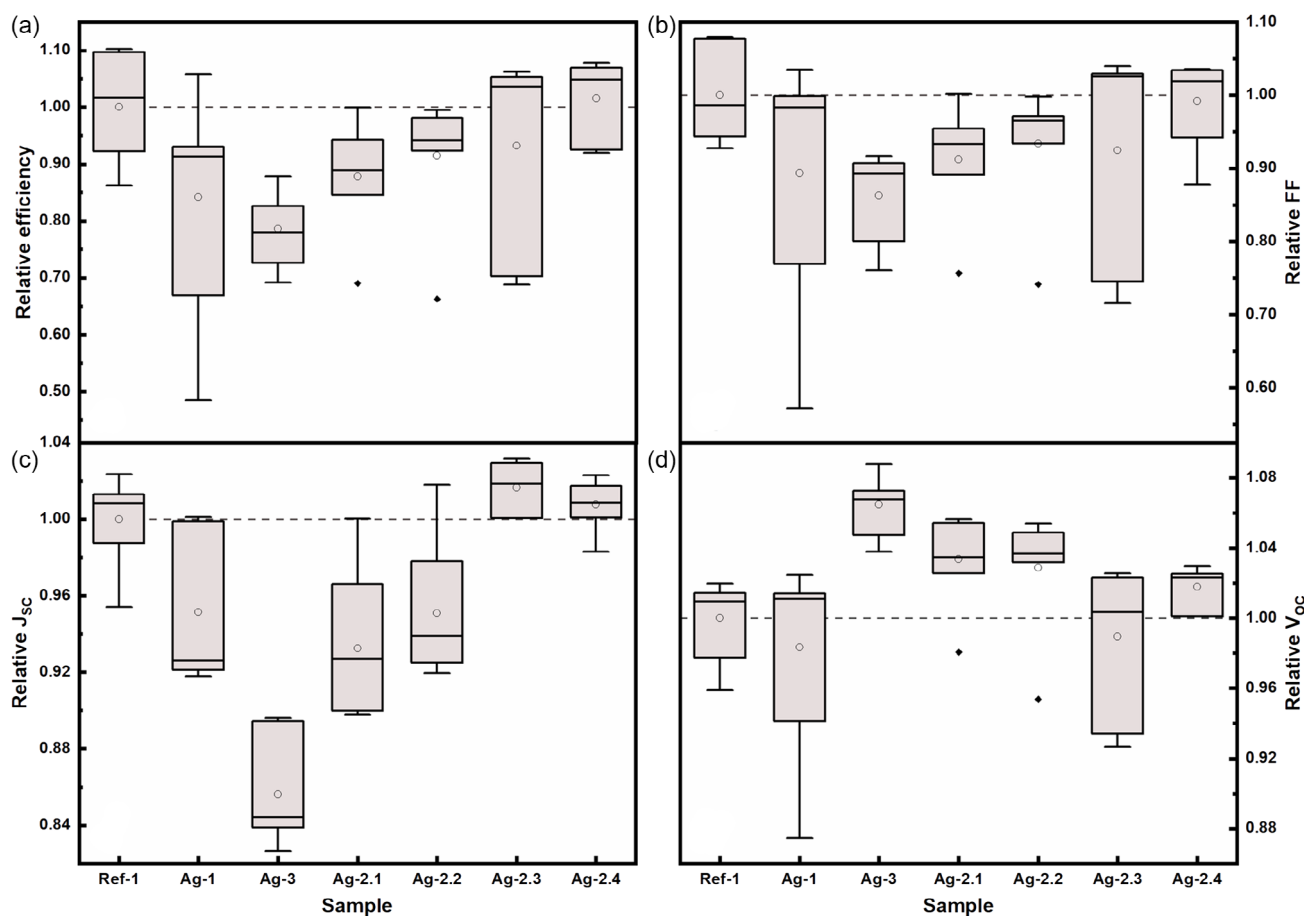


**Figure 6.** Relative *IV* parameters for the cells based on the absorbers discussed in the text. The data are normalized to the mean value of the reference sample. a) The efficiency, b) the FF, c) the  $J_{SC}$ , and d) the  $V_{OC}$  are displayed. For each of the samples, seven different cells are measured. The box limits are given by the first and third quartiles ( $Q_1$  and  $Q_3$ ) and the whiskers by the minimum and maximum values. The dot inside is the mean value and the line is the median. Any data point falling outside  $1.5 \cdot IQR$  is considered an outlier and shown as black dot.  $IQR$  is defined as  $IQR = Q_3 - Q_1$  and stands for interquartile range.

Interestingly, the change in the growth temperature of samples Ag-2.2 and Ag-2.3 did not affect the nonradiative losses. It is therefore possible to obtain similarly good absorbers at a lower process temperature, which might be specifically beneficial for industrial cells due to the cost reduction.

The low energy part of the PL spectrum, far below the bandgap, can be used to measure the tail states.<sup>[37]</sup> Tail states arise from structural disorder, bandgap fluctuations, or electrostatic fluctuations and represent a density of states extending into the forbidden gap. They have a direct detrimental impact on  $V_{OC}$ .<sup>[38–40]</sup> The density of tail states decreases exponentially from the band edge and can be described by the Urbach energy  $E_U$ . A reduction of the Urbach energy upon incorporation of Ag is observed in wide bandgap CIGSe,<sup>[2,5]</sup> but the opposite is reported for low bandgap CIGSe.<sup>[13]</sup> In the present study, no significant change is observed (see Figure 5). The measured  $E_U$  range from 11.4 to 12.0 meV and  $E_U^{Ref} = 11.7$  meV. This suggests that the tail states are not reduced by the Ag incorporation. Another parameter linked to the disorder is the sharpness of the absorption edge. In fact, the PL emission depends on the distribution of bandgaps in the material. For samples without a bandgap gradient, a sharp absorption edge is expected, but with a gradient or if the alloy disorder is increased, the absorption edge becomes less sharp.<sup>[41–43]</sup> Assuming a Gaussian distribution of the energy of step like bandgaps, one can fit the derivative of the absorbance and extract the standard deviation from

$$\frac{dA(E)}{dE} = C_0 + \frac{C_1}{\sigma_{E_g} \cdot \sqrt{2\pi}} \exp\left(-\frac{(E - E_g)^2}{2\sigma_{E_g}^2}\right) \quad (2)$$

where  $A(E)$  is the absorbance (Figure 7),  $E_g$  corresponds to the mean bandgap, and  $\sigma_{E_g}$  is the standard deviation.  $C_0$  and  $C_1$  are

fitting constants. The absorbance is obtained from the PL measurement by solving the generalized Planck's law for  $A(E)$ .<sup>[33,37]</sup>

The standard deviation for each of the samples is reported in Figure 5. The smallest one is obtained for the reference (41 meV) and increases up to 47 meV for the samples Ag-1 and Ag-2.4. Due to the shoulder at 1.25 eV in the PL spectrum, the absorbance of the sample Ag-3—which showed the largest inhomogeneity in the GGI profile and in the Raman spectra—could not be extracted. Such low spreading in the standard deviation (6 meV) is not significant and does not support firm conclusions. The changes observed in the bandgap gradient are too small to have an effect on the broadening. Other effects seem to be more important.

Finally, a decisive parameter for solar cell efficiency is given by the FF. The record CIGS solar cell reaches a FF just above 80%.<sup>[1]</sup> The diode factor is originally defined in the diode equation  $j = j_0 \left( \exp\left(\frac{eV}{A_{el}kT}\right) - 1 \right)$ , where  $j$  is the current density,  $j_0$  is the saturation current density,  $V$  is the voltage,  $e$  is the elementary charge,  $k$  is the Boltzmann constant,  $T$  is the absolute temperature, and  $A_{el}$  is the electrical diode factor (e.g., in ref. [44]). The latter has a direct influence on the FF of the solar cell and takes generally a value between 1 and 2, depending on the recombination mechanism. For a good FF, the diode factor has to be as low as possible. A diode factor larger than 1 is usually considered indicative of recombination in the space charge region (SCR), whereas recombination in the quasineutral region leads to  $A_{el} = 1$ . Empirically, it has been observed that the PL flux  $\phi_{PL}$  depends on the generation flux  $G$  and follows the power law  $\phi_{PL} \propto G^{A_{opt}}$ . Trupke et al.<sup>[45]</sup> and later Babbe et al.<sup>[46]</sup> demonstrate that the exponent  $A_{opt}$  equals the electrical diode factor  $A_{el}$  under two conditions. First, a good collection of the photogenerated charges must be assumed and second, the quasi-Fermi-level splitting measured optically must equal the  $V_{OC}$  of the cell. In

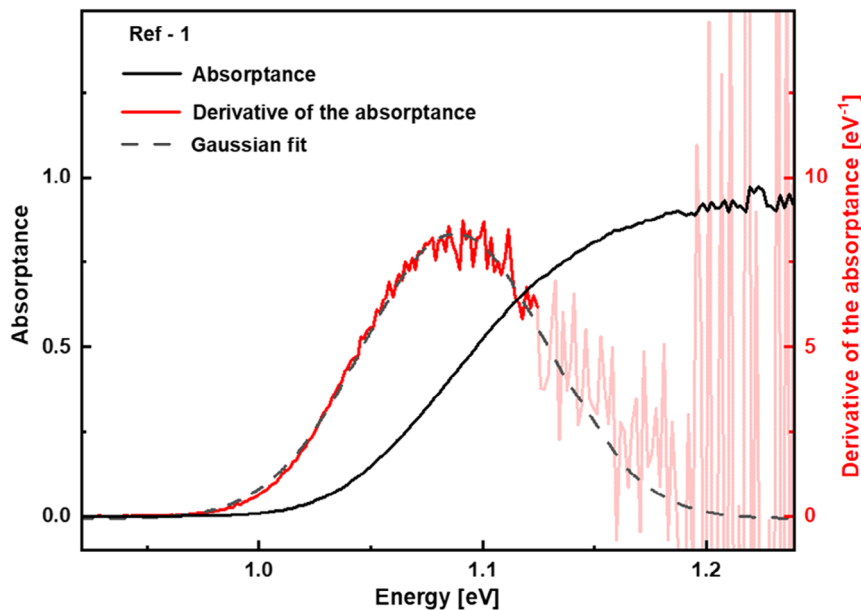


**Figure 7.** Absorbance obtained from a PL measurement on the reference sample (black curve) and its derivative (red curve). The derivative is fitted with Equation (2) (dashed line) over the highlighted range (0.90–1.14 eV). The high energy part of the derivative is disregarded because of the high noise.

all other cases, the electrical diode factor will be larger than the optical one. Measuring excitation-dependent PL thus leads to a determination of the ODF. From the slope of a linear fit in a logarithmic scale, one can read a value for the ODF (see Figure S4, Supporting Information). It is found that upon Ag incorporation, the ODF of the bare absorbers remains unchanged and equals the one of the reference sample,  $ODF = 1.3$ . It is therefore reasonable to expect similar FF for cells prepared from these absorbers, if the subsequent deposited layers (buffer, window layers) are not affected by the different Ag contents themselves. The amount of Ag used in the present absorbers is small enough that no significant change of the band alignment is expected.<sup>[3]</sup>

In the case of a bare absorber—without buffer—there exists no SCR. Weiss et al.<sup>[47,48]</sup> show that an ODF larger than 1 is explained by an additional shift of the majority carriers quasi-Fermi level, even in low injection condition. Upon illumination, metastable defects, like the double vacancy complex  $V_{Se}-V_{Cu}$  in CIGS<sup>[49]</sup>, can change from a donor state to an acceptor state, thus increasing the net acceptor density and in turn shifting the hole quasi-Fermi level closer to the valence band, producing  $ODF > 1$ . Wang et al.<sup>[50]</sup> discuss how increased back surface recombination (nonradiative recombination) and increased doping density (radiative recombination) can lead to lower ODF. The absence of change in the ODF upon Ag alloying, but the slight increase

in PL intensity, may indicate a reduction of surface recombination, together with an improved doping.

#### 2.4. CL Spectroscopy

In the previous section, interdiffusion of Ga and In, as well as lateral inhomogeneity arising upon Ag alloying have been discussed. This section focuses on CL performed on the cross section of the absorber Ag-3 and provides further evidence of the abovementioned observations. A CIGS<sub>Se</sub> sample similar to the reference from this study has already been investigated in another report<sup>[22]</sup> and some of the major results are reproduced in Figure 8. The CL results for the sample Ag-1 can be found in Figure S5.1, Supporting Information. A spectrum is measured for each pixel in the CL measurement, creating a hyperspectral dataset. The corresponding panchromatic emission intensity is depicted in Figure 8b, and the emission energy of the intensity maximum is reported in Figure 8c. It is important at this point to mention that the shown CL measurements were performed using an uncorrected silicon CCD detector. This detector is characterized by a significant reduction in detection efficiency toward the lower measured energies. Measurement performed by an InGaAs diode array, with enhanced sensitivity at the low energy scale can be found in the Figure S5.2,

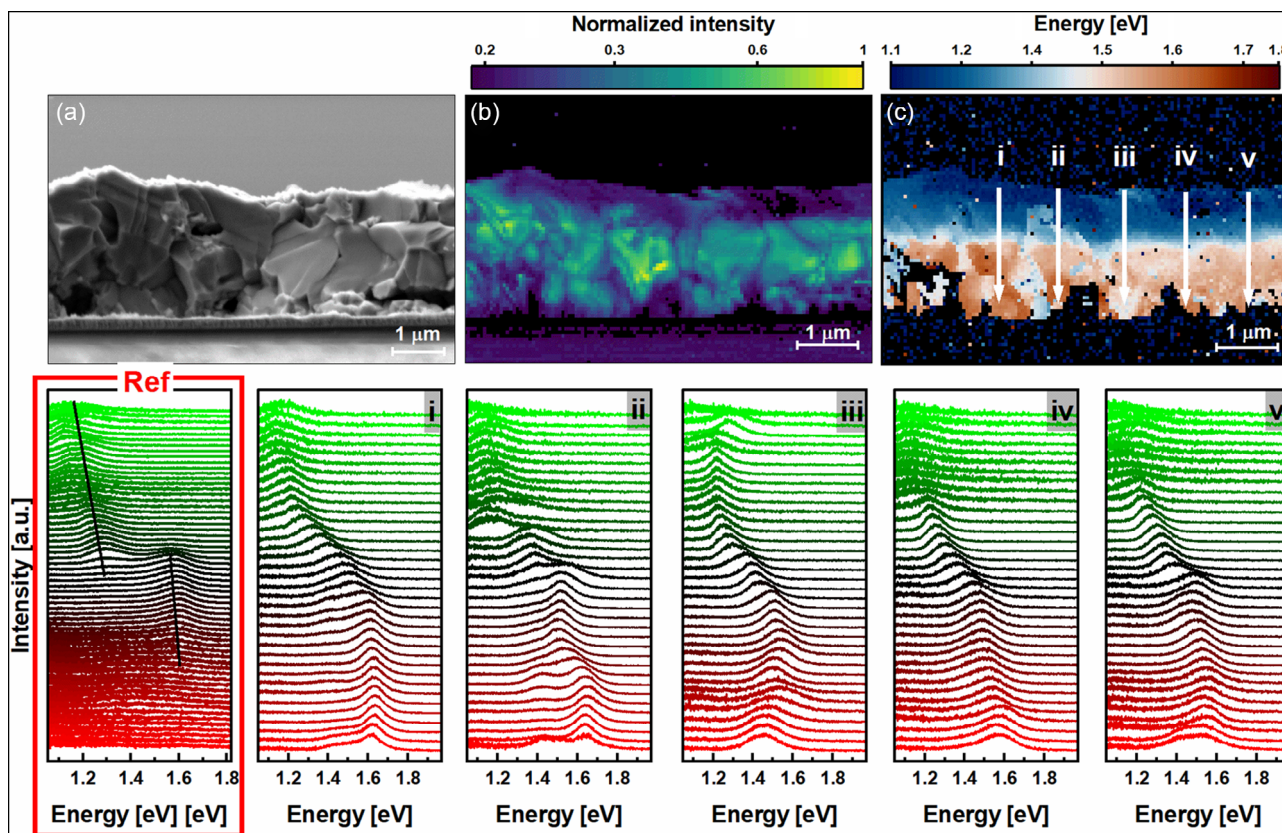


**Figure 8.** CL spectroscopy on the cross section of the sample Ag-3. a) The top row shows the SE image of the region of interest, b) the normalized intensity map of the panchromatic luminescence in logarithmic scale, and c) the colormap of the energy of the maximum of the CL emission. The bottom row shows the individual spectra along the lines i–v drawn in (c). The leftmost graph in the bottom row is reproduced from ref. [22] and corresponds to typical emission observed in the reference sample. The black lines are a guide to the eye. All the spectra are normalized and shifted for clarity.



Supporting Information and shows a brighter front side, as expected. This explains the lower intensity of the signal near the front surface (Figure 8b), as well as the discrepancy between CL and PL about the energy of the luminescence maximum of the low gap phase (1.05 eV from PL and 1.15 eV from CL) because PL utilizes an InGaAs detector in this range. The high energy emission agrees better as both methods use a silicon detector in this range.

Although each pixel in the colormaps is of one single color, the transition from one  $E_g$  to the other is often not sharp and two peaks are visible, but only the energy of the dominant one is displayed.

A sudden jump in emission energy from the low bandgap phase to the high bandgap phase has been the most frequent observation in ref. [22] and an example is given in Figure 8 (red-framed graph). From the front surface toward the back contact,  $E_g$  increases only slightly until a certain depth in the bulk where a jump to a higher  $E_g$  occurs. It is visible from the two peaks present in the spectra at this depth and highlighted by the dark lines. This led to the conclusion that in graded absorbers, there is no smooth bandgap gradient, but instead that a low gap phase forms toward the front, a high gap phase forms toward the back, and the two phases interlace in the bulk of the material.

Similar behavior is observed for the line profile ii in Figure 8, although it is not the most common situation. Indeed, the line profiles i and iii–v reveal a smoother gradient from the front side to the back side, suggesting that Ag increases the gradient behavior, likely by Ga interdiffusion. However, a variation of bandgaps close to the back side is also observed (spectra with two clearly identifiable peaks, e.g., line profiles ii and v). This inhomogeneity is translated in the energy map (Figure 8c) by the abrupt change in color. The lateral inhomogeneity is highlighted by the intermittence of red and light blue close to the back side. Additionally, the first few hundreds of nanometers from the front surface show a mix of dark and lighter blues, indicating the variation of bandgaps as observed from Raman and PL. In particular, patches of higher bandgap are present near the front surface (also visible in the top spectra from the line profile iii in Figure 8). For the sample Ag-1 (lowest Ag content, Figure S5.1, Supporting Information), larger lateral inhomogeneity is observed, and more energy jumps appear in the line profiles.

Taken together, the CL results support the increased diffusion of Ga from the back side toward the front as suggested by the variation of bandgaps near the front and back surfaces. This, in turn, provides the explanation for the flattening of the GGI profiles observed by GDOES. With the formation of higher (lower) bandgap phases near the front (back) surface, the average GGI in this region is expected to increase (decrease). Moreover, with increasing Ag content, a smoother bandgap gradient is achieved, despite a certain lateral inhomogeneity.

### 3. Conclusion

Ag-alloyed industrial chalcopyrites (Ag,Cu)(In,Ga)(S,Se)<sub>2</sub> absorbers have been grown with different (low) Ag contents. It has been found that the crystal morphology improves with Ag, in particular showing an increased grain size. Upon Ag alloying, a stronger interdiffusion of Ga and In is observed, resulting in a redshift of

the high energy peak measured by PL. This correlates with a decrease of the average back side GGI, measured by GDOES. As the back side GGI decreases, the front side GGI increases, leading to a flattening of the GGI profile. The increase of the GGI toward the front side is attributed to the formation of a (A)CIGS<sub>Se</sub> phase of higher Ga content, which is confirmed by Raman spectroscopy. Raman spectroscopy indicates more lateral inhomogeneity with increasing Ag. CL spectroscopy on the cross section of the samples supports the lateral inhomogeneity. However, a smoother bandgap gradient is obtained after Ag alloying compared to the reference. Finally, a reduction of the nonradiative losses of up to 30 meV is measured by PL on the bare absorbers, which translated into a  $V_{OC}$  increase of the corresponding solar cells.

### 4. Experimental Section

**Sample Preparation:** The absorbers investigated in this study are produced in the pilot line of AVANCIS, Germany, according to the SEL-RTP (stack elemental layer followed by rapid thermal processing).<sup>[51,52]</sup> They are grown based on a double barrier back-electrode for the control of alkali-diffusion and Mo selenization. The elemental precursors (Ag)–Cu–In–Ga:Na are sputtered and Se is thermally evaporated. The stack undergoes a rapid thermal process in S atmosphere, completing the formation of the (Ag,Cu)(In,Ga)(S,Se)<sub>2</sub> absorber. The absorbers are grown with same elemental stack precursors but differ in the amount of Ag introduced. The reference sample (AAC = 0) and samples of three different Ag contents are produced. A calibrated X-ray fluorescence investigation indicates that all the investigated absorbers have an overall ratio I/III  $\approx$  0.96. The Ag content is kept low for every variation and does not exceed 10%, i.e., AAC < 0.1. In the following, the names Ag-1 and Ag-3 refer to the lowest and highest Ag content, respectively (see Table 1).

**PL Spectroscopy:** The absorbers are measured by absolute PL spectroscopy. The experimental setup is first calibrated and the resulting spectra are corrected spectrally and in intensity, as described in ref. [22]. Two detectors are utilized to cover a larger spectral window, ranging from 400 to 900 nm using a CCD Si camera (Andor iDus DV420A-OE) and from 900 to 1600 nm using an InGaAs detector (Andor iDus DU490A-1.7). The broadest measured spectrum extends, however, only from 700 to 1600 nm

**Table 1.** List of the samples from this study.

| Sample <sup>a)</sup> | GGI           | AAC                   | Description   |
|----------------------|---------------|-----------------------|---|
| Ref-1                | GGI-3         | No Ag                 | Reference   |
| Ag-1                 |               | AAC-1                 | Lowest AAC  |
| Ag-3                 |               | AAC-3 > AAC-1         | Highest AAC   |
| Ag-2.1               | GGI-2 < GGI-3 | AAC-1 < AAC-2 < AAC-3 | Intermediate AAC<br>Intermediate GGI                          |
| Ag-2.2               | GGI-1 < GGI-2 |                       | Intermediate AAC<br>Lowest GGI                                |
| Ag-2.3               |               |                       | Intermediate AAC<br>Lowest GGI<br>Lower process temperature   |
| Ag-2.4               |               |                       | Intermediate AAC<br>Lowest GGI<br>Lower Na in elemental stack |

<sup>a)</sup>The ((Ag) + [Cu])/([Ga] + [In]) ratio is kept constant for all samples at I/III  $\approx$  0.96.

( $\approx 0.78$  to  $1.77$  eV) as a long-pass filter with cutoff wavelength  $700$  nm is introduced in the setup to protect the detectors from the  $660$  nm wavelength diode laser used as excitation source. If not otherwise stated, the absolute PL measurements are performed under a photon flux of  $2.85 \times 10^{17} \text{ cm}^{-2} \text{ s}^{-1}$ , corresponding to a 1 sun illumination for an absorber of bandgap of  $1.05$  eV based on the AM1.5 g solar spectrum. The numerical results (and error bars) obtained by PL are averaged over three different spots on each absorber. The InGaAs detector used has two diodes of slightly different sensitivity. Therefore, in order to reduce the noise in the PL spectra and corresponding absorbance, only the least noisy of the two is considered.

**CL Spectroscopy:** CL hyperspectral mapping is performed at  $300$  K on a cleaved cross section in an Attolight Allalin 4027 Chronos SEM-CL system. CL measurements are taken using an iHR320 spectrometer with a grating density of  $150$  lines per mm blazed at  $500$  nm. The microscope is operated at an electron beam current of  $2.5$  nA and an electron landing energy  $5$  keV. The CL hyperspectral maps are then analyzed using LumiSpy.<sup>[53]</sup>

**Raman Spectroscopy:** Raman spectroscopy was acquired with a Renishaw inVia micro-Raman spectrometer equipped with a  $532$  nm excitation laser source, a  $100\times$  objective lens (with a numerical aperture of  $0.85$ ) and a  $2400$  lines/mm grating. Several spots are measured in each case, spaced by a few microns.

**SEM:** The morphology and thickness of the bare absorbers were assessed with a Hitachi SU-70 field-emission SEM. Top-view and cross-sectional SEM images were taken with a voltage of  $7$  kV.

## Supporting Information

Supporting Information is available from the Wiley Online Library or from the author.

## Acknowledgements

This work was supported by Avancis, Germany, in the framework of the POLCA project, and by EPSRC in the framework of the REACH project (EP/V029231/1), which are gratefully acknowledged. The authors thank Dr. Mohit Sood for his suggestions and discussion.

## Conflict of Interest

The authors declare no conflict of interest.

## Author Contributions

A.J.-C.M.P.: Conceptualization (equal); investigation (lead); formal analysis (lead); visualization (lead); writing/original draft preparation (lead); writing/review and editing (equal). M.M.: Investigation (supporting); formal analysis (supporting). T.S.: Investigation (supporting). R.G.P.: Investigation (supporting); writing/review and editing (equal). H.E.: Formal analysis (equal); investigation (equal); resources (equal); writing/review and editing (equal). A.L.: Formal analysis (equal); investigation (equal); resources (equal); writing/review and editing (equal). S.O.: Formal analysis (equal); investigation (equal); resources (equal); A.Z.: Formal analysis (equal); investigation (equal); resources (equal); writing/review and editing (equal). T.D.: Formal analysis (equal); resources (equal); writing/review and editing (equal); funding acquisition (lead). G.K.: Formal analysis (equal); investigation (equal); writing/review and editing (equal). Y.H.: Formal analysis (equal); investigation (equal). R.A.O.: Conceptualization (lead); formal analysis (equal); writing/review and editing (equal); funding acquisition (lead). S.S.: Conceptualization (lead); formal analysis (equal); funding acquisition (equal); supervision (lead); writing/review and editing (equal).

## Data Availability Statement

The data that support the findings of this study are openly available in Zenodo at <https://doi.org/10.5281/zenodo.10686926>, reference number 10686926.

## Keywords

cathodoluminescence spectroscopy, chalcopyrite solar cells, industrial processes, photoluminescence spectroscopy, silver alloying

Received: March 12, 2024

Revised: April 20, 2024

Published online:

- [1] J. Keller, K. Kiselman, O. Donzel-Gargand, N. M. Martin, M. Babucci, O. Lundberg, E. Wallin, L. Stolt, M. Edoff, *Nat. Energy* **2024**, 9, 467.
- [2] P. T. Erslev, G. M. Hanket, W. N. Shafarman, J. David Cohen, *Mater. Res. Soc.* **2009**, 1165, 107.
- [3] J. Keller, K. V. Sopiha, O. Stolt, L. Stolt, C. Persson, J. J. S. Scragg, T. Törndahl, M. Edoff, *Prog. Photovoltaics: Res. Appl.* **2020**, 28, 237.
- [4] T. Nakada, K. Yamada, R. Arai, H. Ishizaki, N. Yamada, *MRS Proc.* **2005**, 111, 865.
- [5] P. T. Erslev, J. Lee, G. M. Hanket, W. N. Shafarman, J. D. Cohen, *Thin Solid Films*, **2011**, 519, 7296.
- [6] K. Kim, J. W. Park, J. S. Yoo, J. S. Cho, H. D. Lee, J. H. Yun, *Sol. Energy Mater. Sol. Cells* **2016**, 146, 114.
- [7] J. Keller, P. Pearson, N. Shariati Nilsson, O. Stolt, L. Stolt, M. Edoff, *Sol. RRL* **2021**, 5, 2100403.
- [8] G. M. Hanket, C. P. Thompson, J. K. Larsen, E. Eser, W. N. Shafarman, *38th IEEE Photovoltaic Specialists Conf.*, Austin, TX, USA, **2012**.
- [9] L. Chen, J. Lee, W. N. Shafarman, *IEEE J. Photovoltaics* **2014**, 4, 447.
- [10] M. Edoff, T. Jarmar, N. S. Nilsson, E. Wallin, D. Hogstrom, O. Stolt, O. Lundberg, W. Shafarman, L. Stolt, *IEEE J. Photovoltaics* **2017**, 7, 1789.
- [11] N. Valdes, J. Lee, W. Shafarman, in *IEEE 7th World Conf. on Photovoltaic Energy Conversion (WCPEC)*, Waikoloa, HI **2018**.
- [12] N. Valdes, J. W. Lee, W. Shafarman, *Sol. Energy Mater. Sol. Cells* **2019**, 195, 155.
- [13] A. Kanevce, S. Essig, S. Paetel, W. Hempel, D. Hariskos, T. Magorian Friedlmeier, *EPJ Photovoltaics* **2022**, 13, 28.
- [14] C. Wang, Z. Hu, Y. Liu, S. Cheng, Y. Yao, Y. Zhang, X. Yang, Z. Zhou, F. Liu, Y. Zhang, Y. Sun, W. Liu, *J. Mater. Sci.: Mater. Electron.* **2022**, 33, 11055.
- [15] J. L. Shay, J. H. Wernick, in *Ternary Chalcopyrite Semiconductors: Growth, Electronic Properties, and Applications*, Pergamon Press, New York, **1975**.
- [16] Y. Zhang, L. Shi, Z. Wang, H. Dai, Z. Hu, S. Zhou, H. Chen, X. Feng, J. Zhu, Y. Sun, W. Liu, Q. Zhang, *Sol. Energy* **2021**, 227, 334.
- [17] M. Krause, S. C. Yang, S. Moser, S. Nishiwaki, A. N. Tiwari, R. Carron, *Sol. RRL* **2023**, 7.
- [18] Y. Zhao, S. Yuan, D. Kou, Z. Zhou, X. Wang, H. Xiao, Y. Deng, C. Cui, Q. Chang, S. Wu, *ACS Appl. Mater. Interfaces* **2020**, 12, 12717.
- [19] H. Mori, J. Chantana, Y. Kawano, T. Negami, T. Minemoto, *Mater. Sci. Eng.: B* **2023**, 297, 116758.
- [20] K. Cheng, X. Shen, J. Liu, X. Liu, Z. Du, *Sol. Energy* **2021**, 217, 70.
- [21] S. Essig, S. Paetel, T. M. Friedlmeier, M. Powalla, *J. Phys. Mater.* **2021**, 4, 024003.

- [22] A. J. C. M. Prot, M. Melchiorre, F. Dingwell, A. Zelenina, H. Elanzeery, A. Lomuscio, T. Dalibor, M. Guc, R. Fonoll-Rubio, V. Izquierdo-Roca, G. Kusch, R. A. Oliver, S. Siebentritt, *APL Mater.* **2023**, *11*, 101120.
- [23] G. Kim, W. M. Kim, J. K. Park, D. Kim, H. Yu, J. H. Jeong, *ACS Appl. Mater. Interfaces* **2019**, *11*, 31923.
- [24] H. Rodriguez-Alvarez, R. Mainz, R. Caballero, D. Abou-Ras, M. Klaus, S. Gledhill, A. Weber, C. A. Kaufmann, H. W. Schock, *Sol. Energy Mater. Sol. Cells* **2013**, *116*, 102.
- [25] D. J. Schroeder, G. D. Berry, A. A. Rockett, *Appl. Phys. Lett.* **1996**, *69*, 4068.
- [26] D. Colombara, *Phys. Rev. Mater.* **2019**, *3*, 054602.
- [27] F. Oliva, S. Kretzschmar, D. Colombara, S. Tombolato, C. M. Ruiz, A. Redinger, E. Saucedo, C. Broussillou, T. G. de Monsabert, T. Unold, P. J. Dale, V. Izquierdo-Roca, A. Pérez-Rodríguez, *Sol. Energy Mater. Sol. Cells* **2016**, *158*, 168.
- [28] S. Y. Kim, M. S. Mina, J. Lee, J. H. Kim, *ACS Appl. Mater. Interfaces* **2019**, *11*, 45702.
- [29] C. Insignares-Cuello, C. Broussillou, V. Bermúdez, E. Saucedo, A. Pérez-Rodríguez, V. Izquierdo-Roca, *Appl. Phys. Lett.* **2014**, *105*, 021905.
- [30] J. Keller, L. Stolt, K. V. Sopiha, J. K. Larsen, L. Riekehr, M. Edoff, *Sol. RRL* **2020**, *4*, 2000508.
- [31] Y. H. Chang, R. Carron, M. Ochoa, C. Bozal-Ginesta, A. N. Tiwari, J. R. Durrant, L. Steier, *Adv. Energy Mater.* **2021**, *11*, 2003446.
- [32] S. Siebentritt, T. P. Weiss, M. Sood, M. H. Wolter, A. Lomuscio, O. Ramirez, *J. Phys. Mater.* **2021**, *4*, 042010.
- [33] S. Siebentritt, U. Rau, S. Gharabeiki, T. P. Weiss, A. Prot, T. Wang, D. Adeleye, M. Drahem, A. Singh, *Faraday Discuss* **2022**, *239*, 112.
- [34] W. Shockley, H. J. Queisser, *J. Appl. Phys.* **1961**, *32*, 510.
- [35] S. Rühle, *Sol. Energy* **2016**, *130*, 139.
- [36] C. Spindler, D. Regesch, S. Siebentritt, *Appl. Phys. Lett.* **2016**, *109*, 032105.
- [37] G. Rey, C. Spindler, F. Babbe, W. Rachad, S. Siebentritt, M. Nuys, R. Carius, S. Li, C. Platzer-Björkman, *Phys. Rev. Appl.* **2018**, *9*, 064008.
- [38] M. H. Wolter, R. Carron, E. Avancini, B. Bissig, T. P. Weiss, S. Nishiwaki, T. Feurer, S. Buecheler, P. Jackson, W. Witte, S. Siebentritt, *Prog. Photovoltaics: Res. Appl.* **2021**, *30*, 702.
- [39] O. Ramírez, J. Nishinaga, F. Dingwell, T. Wang, A. Prot, M. H. Wolter, V. Ranjan, S. Siebentritt, O. Ramírez, F. Dingwell, T. Wang, A. Prot, M. H. Wolter, V. Ranjan, S. Siebentritt, J. Nishinaga, *Sol. RRL* **2023**, *7*, 2300054.
- [40] S. De Wolf, J. Holovsky, S. J. Moon, P. Löper, B. Niesen, M. Ledinsky, F. J. Haug, J. H. Yum, C. Ballif, *J. Phys. Chem. Lett.* **2014**, *5*, 1035.
- [41] U. Rau, J. H. Werner, *Appl. Phys. Lett.* **2004**, *84*, 3735.
- [42] J. Mattheis, U. Rau, J. H. Werner, *J. Appl. Phys.* **2007**, *101*, 113519.
- [43] S. Gharabeiki, T. Schaff, F. Lodola, T. Wang, S. Siebentritt, (In preparation) **2024**.
- [44] R. Scheer, H. W. Schock, in *Chalcogenide Photovoltaics Physics, Technologies, and Thin Film Devices*, Wiley-VCH Verlag GmbH & Co, Weinheim, **2011**.
- [45] T. Trupke, R. A. Bardos, M. D. Abbott, J. E. Cotter, *Appl. Phys. Lett.* **2005**, *87*, 093503.
- [46] F. Babbe, L. Choubrac, S. Siebentritt, *Sol. RRL* **2018**, *2*, 1800248.
- [47] T. P. Weiss, F. Ehre, V. Serrano-Escalante, T. Wang, S. Siebentritt, *Sol. RRL* **2021**, *5*, 2100063.
- [48] T. P. Weiss, O. Ramírez, S. Paetel, W. Witte, J. Nishinaga, T. Feurer, S. Siebentritt, *Phys. Rev. Appl.* **2023**, *19*, 024052.
- [49] S. Lany, A. Zunger, *J. Appl. Phys.* **2006**, *100*, 113725.
- [50] T. Wang, F. Ehre, T. P. Weiss, B. Veith-Wolf, V. Titova, N. Valle, M. Melchiorre, O. Ramírez, J. Schmidt, S. Siebentritt, *Adv. Energy Mater.* **2022**, *12*, 2202076.
- [51] J. Palm, T. Dalibor, R. Lechner, S. Pohlner, R. Verma, R. Dietmüller, A. HeiB, H. Vogt, F. Karg, in *29th European Photovoltaic Solar Energy Conf. and Exhibition*, Amsterdam, The Netherlands **2014**.
- [52] H. Elanzeery, M. Stölzel, P. Eraerds, P. Borowski, H. Aboulfadl, A. Lomuscio, D. Helmecke, C. Schubert, S. Oueslati, M. Hala, J. Röder, F. Giesl, T. Dalibor, *IEEE J. Photovolt* **2023**, *14*, 107.
- [53] J. Lähnemann, J. F. Orri, E. Prestat, D. N. Johnstone, N. Tappy, LumiSpy/lumispy: v0.2.1 **2022**.